Supplementary Information (SI) for Journal of Materials Chemistry A.

Supplementary Information

Controlling the ratio of Ni and Fe co–doping in Prussian–White cathode to improve the structural stability and redox performance of advanced sodium–ion batteries†

Dae Hyun Lee [a, ‡], Love Kumar Dhandole [a, ‡], Su Hyeon Ahn [a,c], Mahadeo A. Mahadik [d], Hyeon Ih Ryu [e], Hee-Suk Chung [f], Hyun Gyu Kim [g], Du Hyun Lim [c,*], Jum Suk Jang [a,b*]

a. Department of Integrative Environmental Biotechnology, College of Environmental and Bioresource Sciences, Jeonbuk National University, Iksan 54596, Republic of Korea

b. Division of Biotechnology, College of Environmental and Bioresource Sciences, Jeonbuk National University, Iksan 54596, Republic of Korea

c. Energy 11. Co. Ltd, 122 Bongdong–eup, Wanjusandan 9–ro, Wanju–Gun, Jeollabuk–do, 55315, Republic of Korea

d. School of Civil and Environmental Engineering, Cornell University, Ithaca, NY 14853, USA

e. AI enhanced Electron Microscopy Group, Korea Basic Science Institute, Daejeon 34133, Republic of Korea

f. Research Center for Materials Analysis, Korea Basic Science Institute, Daejeon 34133, Republic of Korea

g. Busan Center, Korea Basic Science Institute (KBSI), Busan 46742, Republic of Korea

*Corresponding authors.

‡ Equal contributions

† Supplementary Information available

E–mail address: duhyun@energy11.co.kr (D. H. Lim), jangjs75@jbnu.ac.kr (J. S. Jang)

Table. S1. Particle surface elemental distribution of MNFHCF–631 confirmed by EDAX APEX.

Elements	Wt %	Atomic %
C	27.9	39.5
N	31.3	38.0
O	8.4	9.0
Na	8.4	6.2
Mn	8.8	2.7
Fe	11.4	3.5
Ni	3.8	1.1

Table. S2. Elemental distribution of MNFHCF–631 confirmed by TEM mapping EDS.

Elements	**Wt %**	**Atomic %**
C	24.74	39.35
N	27.83	37.96
Na	13.46	11.18
Mn	7.16	2.49
Fe	17.21	5.89
Ni	9.61	3.13

Table. S3. ICP-OES results of prepared samples. The data is given in (wt %).

Sample	Na	Mn	Ni	Fe
bare	13.5	18.4	0	16.2
MNFHCF-631	13.1	14.2	4.3	18.3

Table. S4. Chemical composition based on ICP-OES results of prepared samples. The data is given in mole (stoichiometric ratios).

Sample	Na	Mn	Ni	Fe
bare	1.77	0.99	0	0
MNFHCF-631	1.71	0.778	0.21	0.06

Table. S5. EIS fitting parameters of MHCF, MNFHCF–631, MNFHCF–721, MNFHCF–811 before cycling.

Samples	**R_s**	**R_{ct}**	**CPE_{ct}**	**W_i**
MHCF	3.54	804.60	4.09	2180.00
MNFHCF–811	3.53	1237.00	6.24	2056.00
MNFHCF–721	4.28	1903.00	4.18	1877.00
MNFHCF–631	15.84	1813.00	5.09	2939.00

data is given in R_s, R_{ct} in Ohm (Ω), CPE (μF), W_i Warburg element (Ω).

Table. S6. EIS fitting parameter of MHCF, MNFHCF–631 before and after cycling.

Samples	**R_s**	**R_{CEI}**	**R_{ct}**	**CPE_{ct}**	**CPE_{CEI}**	**W_i**
i. Before cycling – MHCF	3.54	–	804.60	4.09	–	2180.00
ii. After cycling – MHCF	12.38	597.20	161.40	9.23	330.00	57.38
iii. Before cycling – MNFHCF-631	15.84	–	1813.00	5.09	–	2939.00
iv. After cycling – MNFHCF-631	11.63	555.90	95.39	9.79	21.78	143.10

data is given in R_s, R_{ct} in Ohm (Ω), CPE (μF), W_i Warburg element (Ω).

Table. S7. Specific capacity retention rates.

Mn:Ni:Fe ratios	Initial capacity (mAh/g)	After 100 cycles capacity retention (%)
MHCF	97.90	38.52
6:4:0	77.01	86.05
6:0:4	105.10	60.58
6:3:1	**90.06**	**96.30**
7:2:1	85.82	80.17
8:1:1	93.51	53.84
5:4:1	75.49	76.79
5:3:2	83.96	84.92

Table. S8. List of the cycling performance of the representative transition metal doped Mn based Prussian blue analogues.

Samples	Current density	Initial capacity [mAh g^{-1}]	Capacity retention [%]	Cycles	Refs.
$Na_{1.55}Mn_{0.96}Co_{0.04}[Fe(CN)_6]_{0.88}\cdot 0.14H_2O$	1C	121.59	60.14	300	[1]
$Na_{1.58}Mn_{0.78}Zn_{0.22}[Fe(CN)_6]_{0.84}\cdot 2.66H_2O$	750 mA/g	66.9	65	2000	[2]
C2-NaMn (Sn doping)	2C	89.93	80.5	100	[3]
$Na_{1.02}Mn_{0.57}Fe_{0.43}[Fe(CN)_6]_{0.63}\cdot 1.39H_2O$	100 mA/g	120	86	200	[4]
$K_{1.16}Mn_{0.9}Cu_{0.06}Ni_{0.07}[Fe(CN)_6]_{0.96}\cdot 0.47H_2O$	0.1 A/g	100.1	81.8	500	[5]
$K_{1.95}Na_{0.05}Ni_{0.02}Mn_{0.93}[Fe(CN)_6]\square_{0.05}\cdot 0.41H_2O$	0.5C	(max) 101	80	100	[6]
MNFHCF-631	**0.2 C**	**90.17**	**96.30**	**100**	**This work**
MNFHCF–631	**1C**	**77.50**	**79.76**	**100**	**This work**

Table. S9. Elemental composition of MHCF, MNFHCF–631, MNFHCF–721, MNFHCF–811 by XPS analysis.

Samples		C	N	O	Mn	Fe	Ni
i.	**MHCF**	45.50	35.90	9.40	3.25	2.3	0.00
ii.	**MNFHCF–811**	45.55	33.10	11.25	2.85	2.65	0.20
iii.	**MNFHCF–721**	48.70	33.00	11.10	1.65	1.80	0.35
iv.	**MNFHCF–631**	50.75	26.42	12.93	2.17	5.38	2.35

data is given in atomic ratio (At %).

Table. S10. XPS deconvolution fitting peaks binding energies of MHCF, MNFHCF–631.

Orbits	Samples	Binding energy (eV)	Area	Chemical state
Fe 2p	MHCF	708.60	7796.515	Fe^{2+}
		709.70	837.822	Fe^{3+}
		721.52	4016.656	Fe^{2+}
		723.10	1850.955	Fe^{3+}
Fe 2p	MNFHCF–631	708.67	8828.894	Fe^{2+}
		709.700	524.000	Fe^{3+}
		721.51	4336.386	Fe^{2+}
		723.56	413.735	Fe^{3+}
Mn 2p	MHCF	641.20	5147.441	Mn^{2+}
		642.90	3280.541	Mn^{3+}
		653.50	2151.967	Mn^{2+}
		654.90	1893.766	Mn^{3+}
Mn 2p	MNFHCF–631	641.26	5605.613	Mn^{2+}
		642.78	2320.760	Mn^{3+}
		653.30	889.850	Mn^{2+}
		654.85	395.878	Mn^{3+}
O 1s	MHCF	530.13	2459.877	Metal–O
		531.32	2030.746	Metal–OH
		534.89	6346.359	Surface/intersitial H_2O
		535.90	3145.886	Adsorbed H_2O
O 1s	MNFHCF–631	531.71	2948.351	Metal–O
		533.56	1422.956	Metal–OH
		535.57	2678.870	Surface/intersitial H_2O
		536.86	1422.956	Adsorbed H_2O

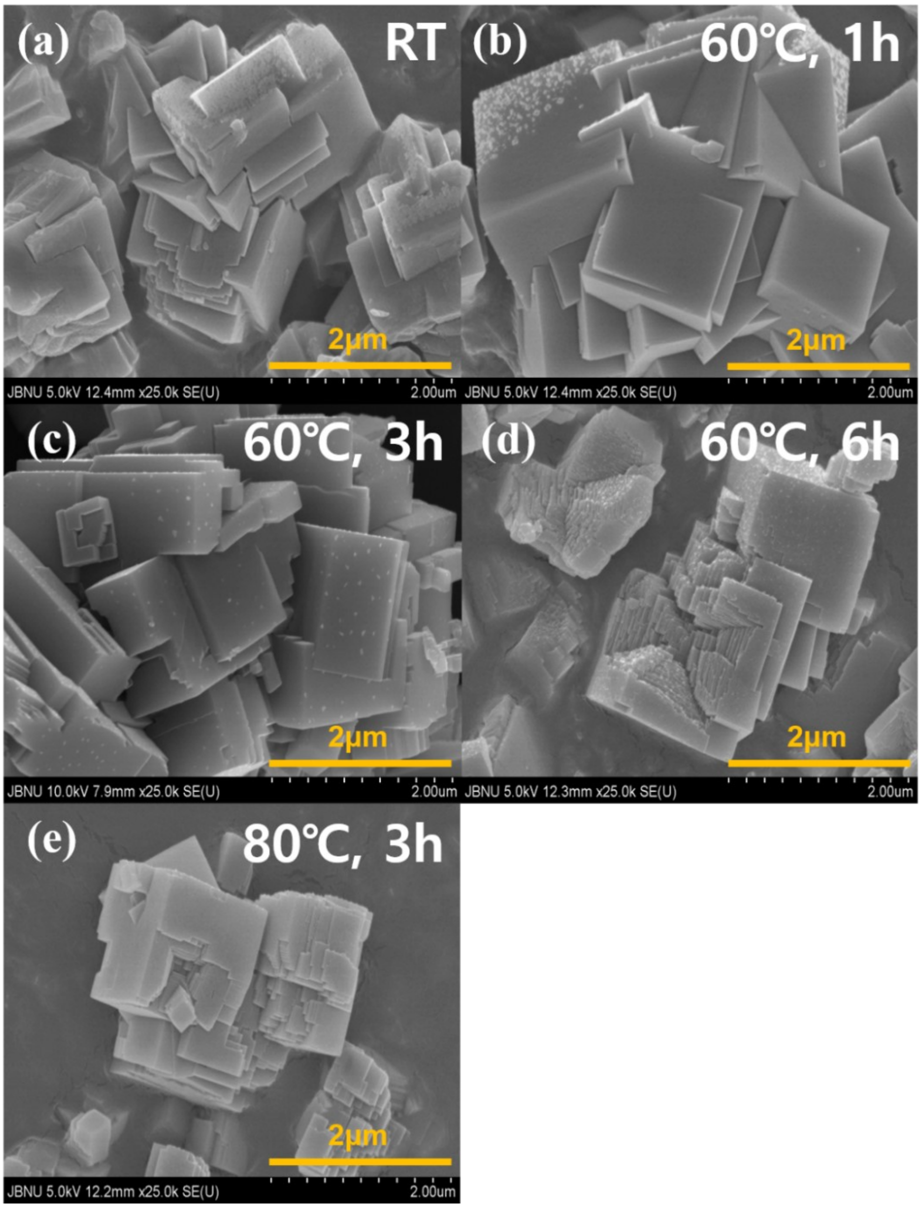

Figure. S1. FESEM images of particles in the electrode of (a) room temperature, (b) 60 °C for 1 h, (c) 60 °C for 3 h, (d) 60 °C for 6 h, and (e) 80 °C for 3 h.

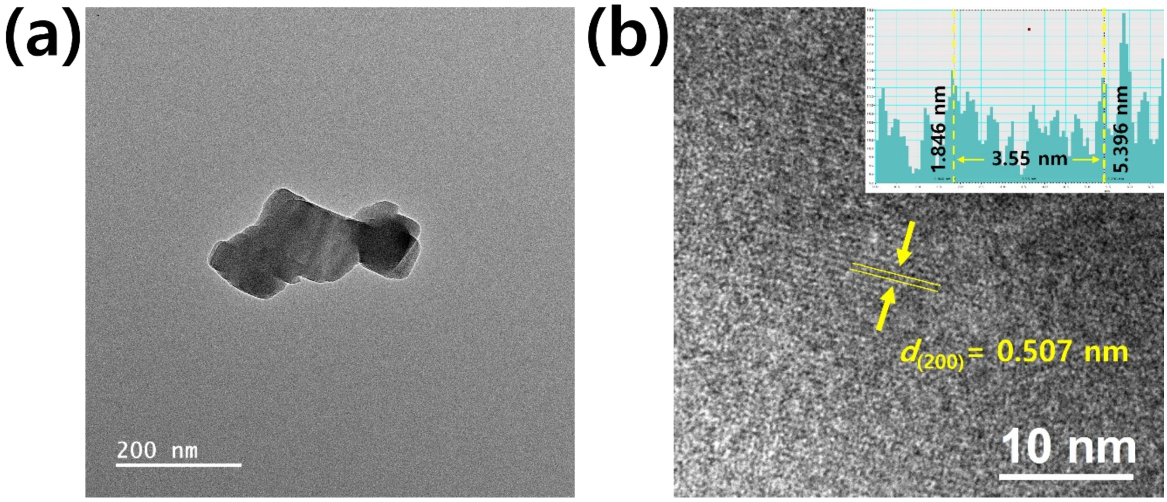

Figure. S2. (a) TEM images, (b) HR−TEM images of the MHCF.

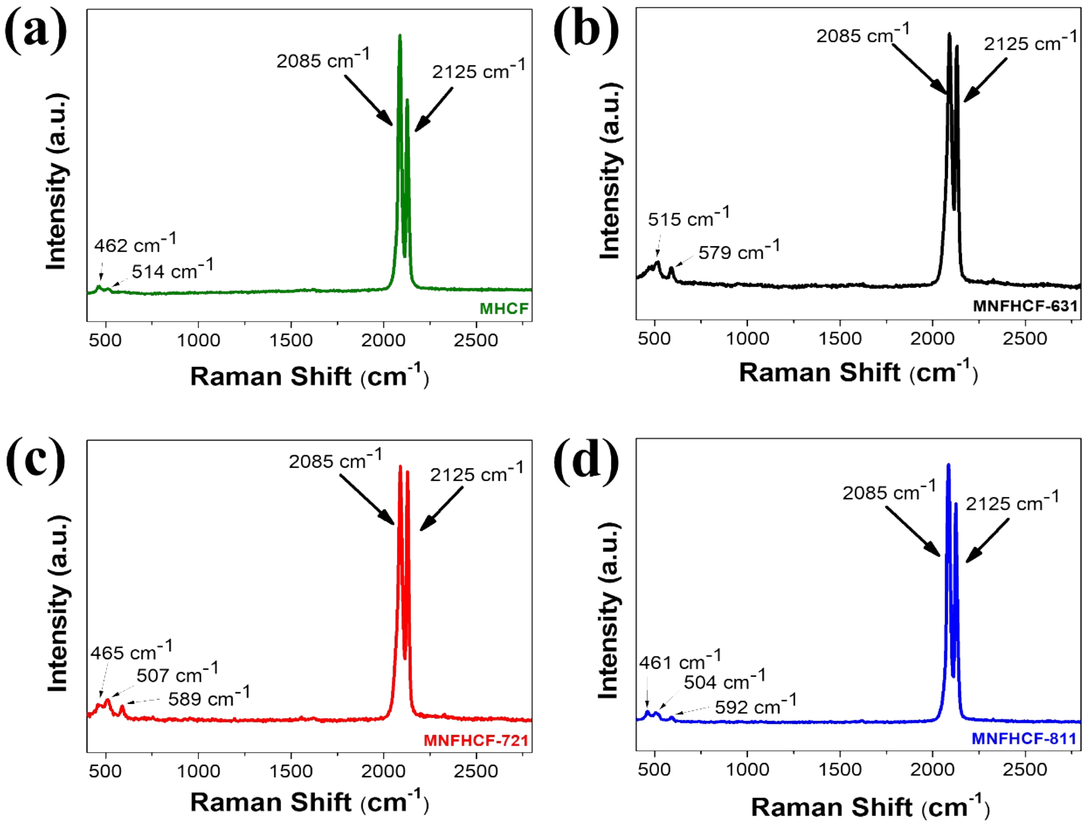

Figure. S3. Raman spectra of the (a) MHCF, (b) MNFHCF–631, (c) MNFHCF–721, (d) MNFHCF–811.

The ratio of the peak at 2085 cm^{-1} to the peak at 2125 cm^{-1} is calculated to be 1.32, 1.05, 1.02, and 1.17 for MHCF, MNFHCF–631, MNFHCF–721, and MNFHCF–811 samples, respectively, and the ratio approaches 1 in samples with high nickel content. This means that the higher intensity of the 2125 cm^{-1} peak as the nickel doping content increases indicates that the bonding strength of the cyanide group increases due to nickel doping, which makes the lattice more rigid and effectively suppresses the Jahn–Teller effect.

Previously reported papers have explained that partial substitution of nickel reduces the axial distance in the MnN$_6$ octahedron, thereby increasing the covalent nature of the Mn–N bond.[7] Similarly, the increase in intensity at 2125 cm^{-1} after nickel doping in our material indicates an increase in the covalent nature, which can be inferred to have stabilized the lattice and improved the performance of the cathode material.

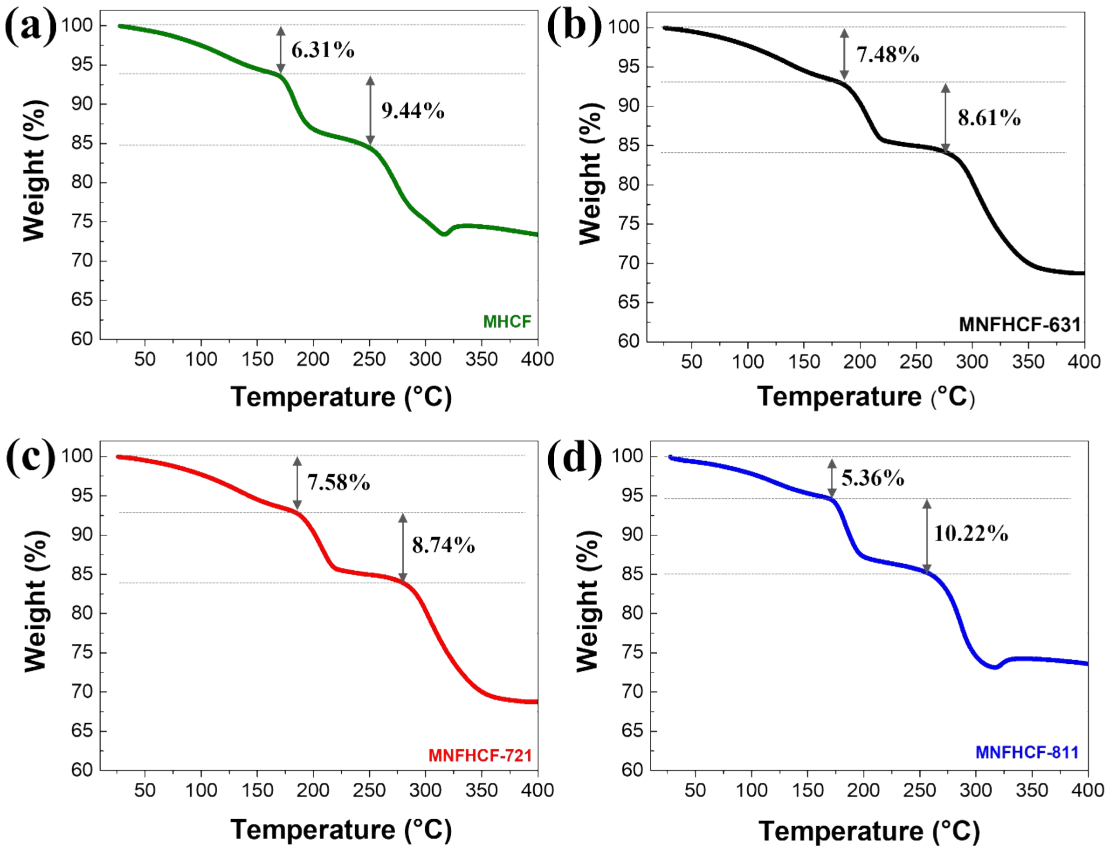

Figure. S4. TGA curve of the (a) MHCF, (b) MNFHCF–631, (c) MNFHCF–721(d) MNFHCF–811.

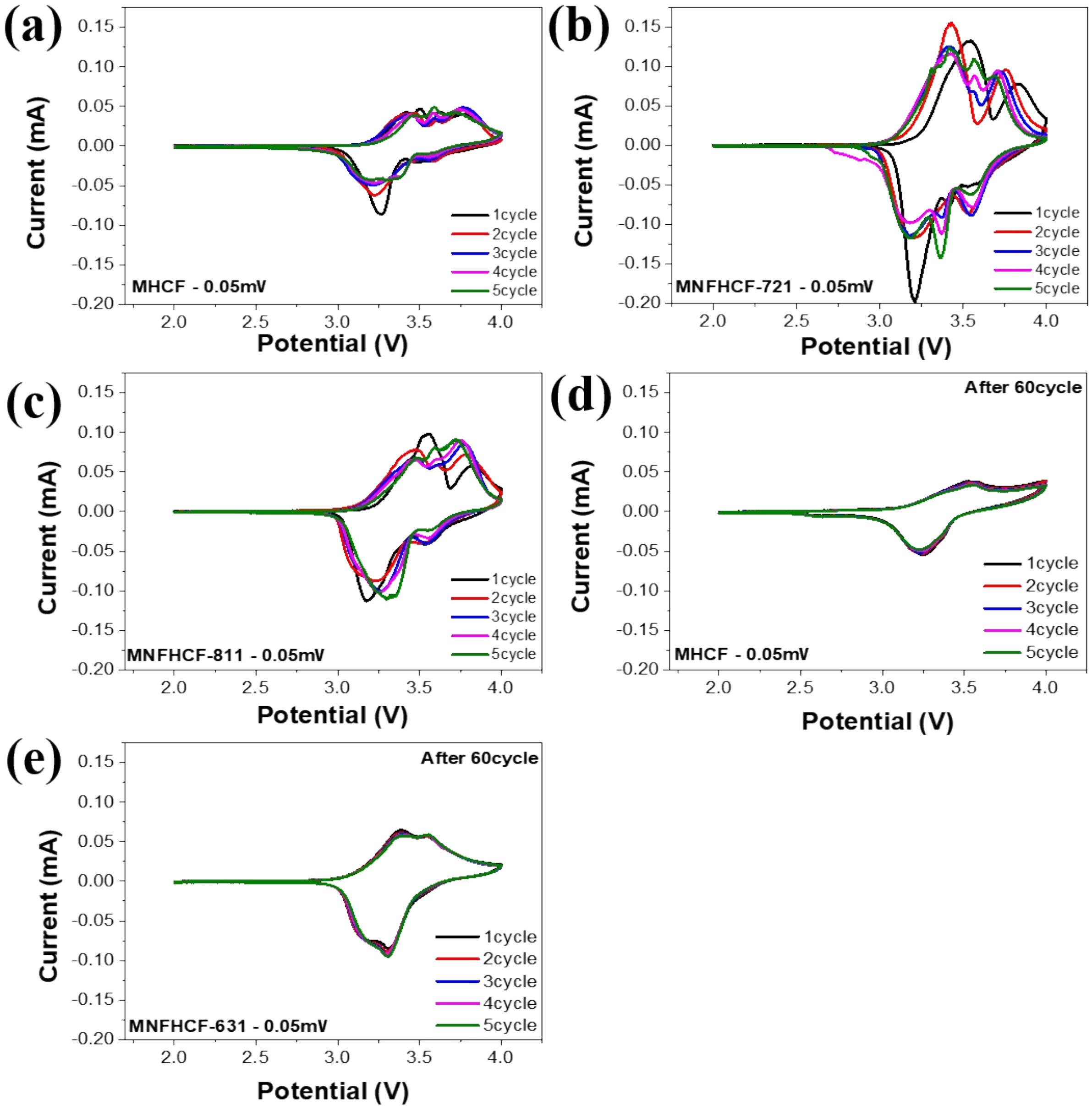

Figure. S5. CV curves of (a) MHCF (b) MNFHCF–721 (c) MNFHCF–811 electrodes at 0.05 mV, CV curve at 0.05 mV after 60 cycles of (d) MHCF (e) MNFCF–631 electrode.

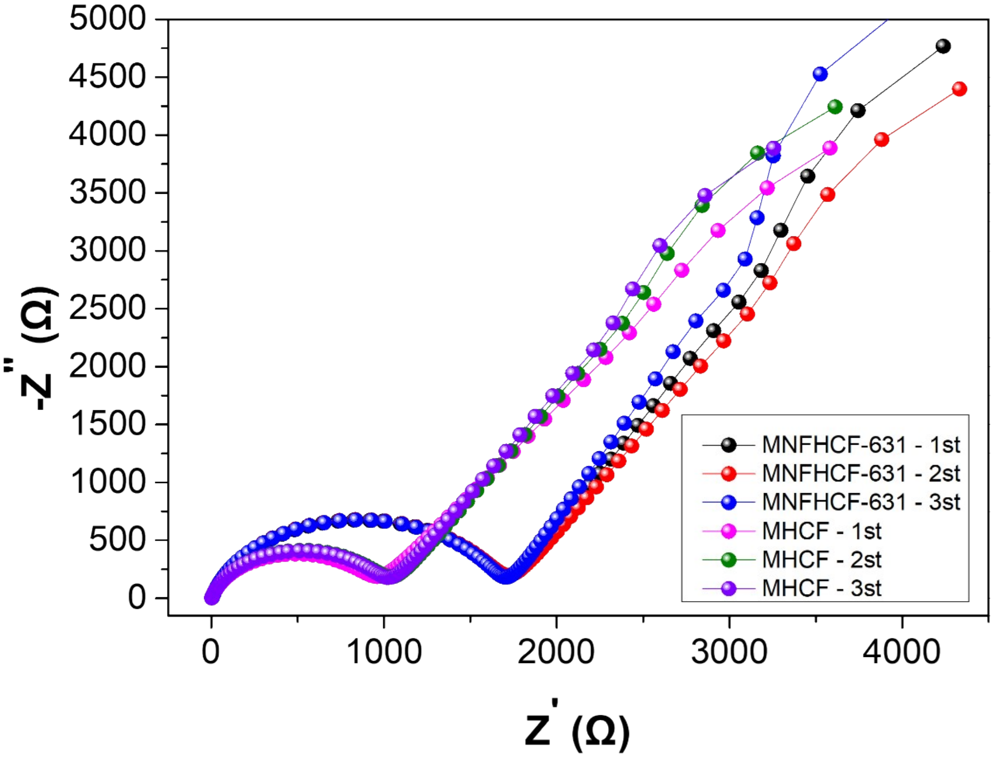

Figure. S6. Results of repeated EIS measurements before cycling.

The EIS measurements of MHCF and MNFHCF–631 were repeated several times before cycling. However, MNFHCF–631 consistently exhibited larger semicircles. This behavior is attributed to lattice contraction caused by nickel doping, which not only inactive electrochemically, as well as hinders ion transport at the particle surfaces before cycling. XPS atomic% and weight% analyses confirm that nickel is primarily located at the surface (Table S6).

From the cycling test results it is found that after cycling, the electrode becomes activated and stabilized, resulting in a decrease in initially high resistance. Unlike MHCF, MNFHCF–631 exhibits minimal structural change (Fig. S11), which enables the stable formation of a CEI layer on the electrode surface during charge–discharge processes. This uniform and robust CEI layer effectively protects the electrode, enhances interfacial stability, and facilitates more easy ion transport. In contrast, MHCF undergoes significant phase transitions, leading to uneven CEI formation caused by repeated decomposition and reformation of the interface. As a result, cracks develop at the interface, increasing resistance and deteriorating electrochemical performance. As reported previously, ion diffusion can be hindered when the nickel content exceeds 10%, leading to increased resistance.[8]

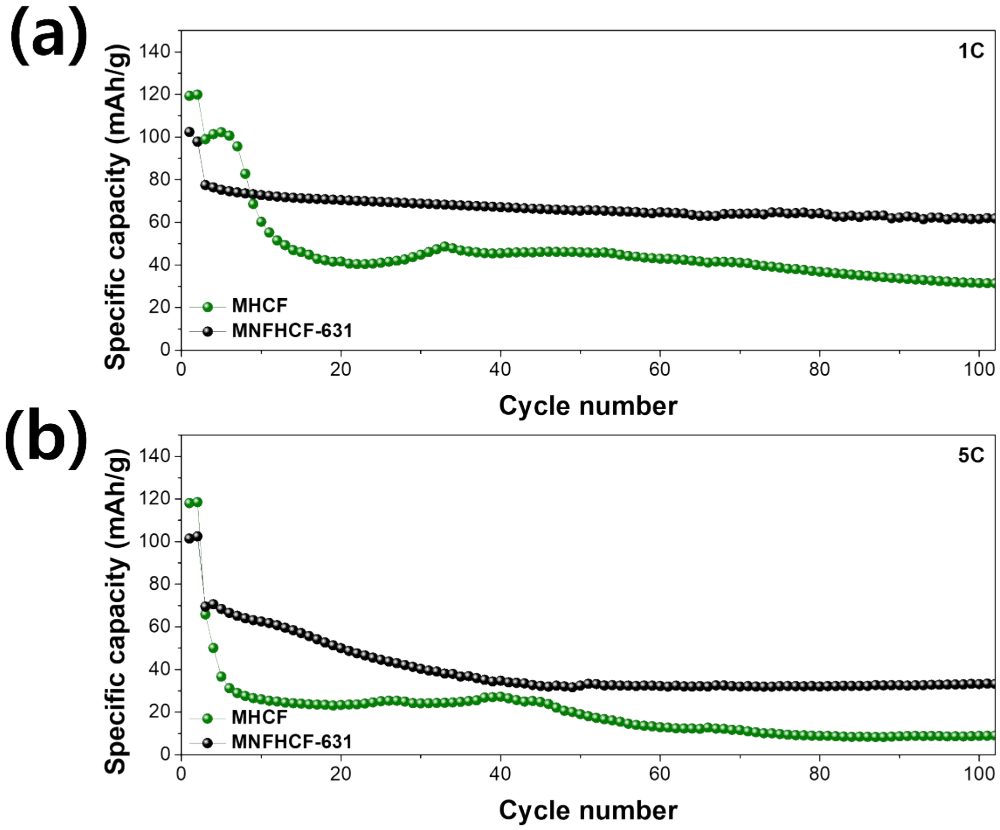

Figure. S7. Cycling performance at (a) 1 C, and (b) 5C of MHCF and MNFHCF–631.

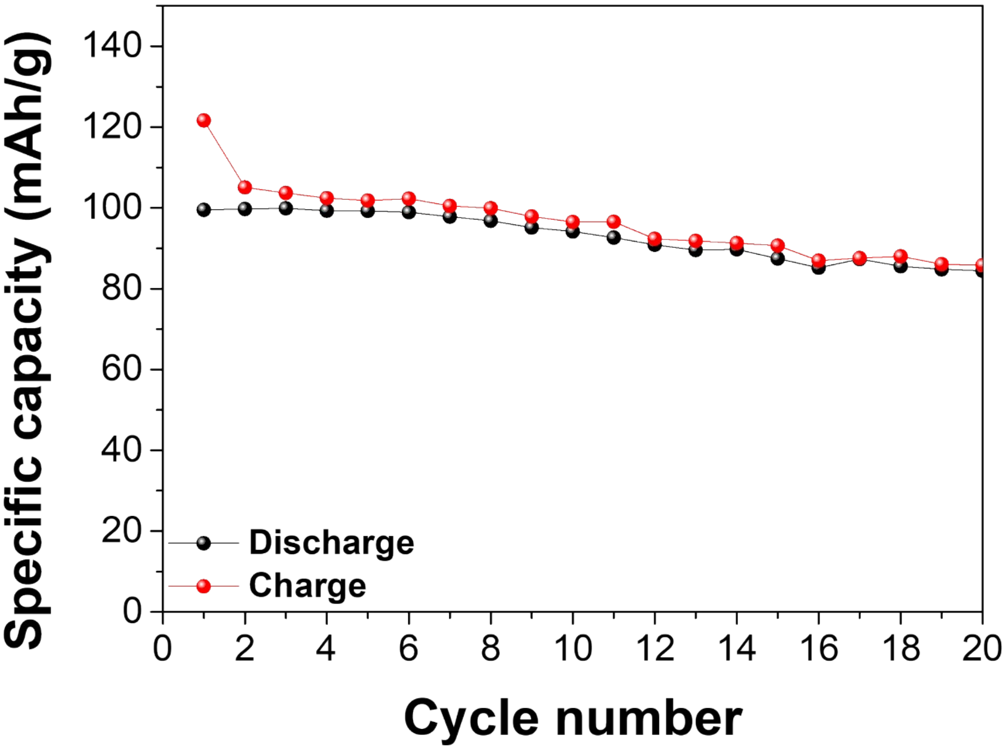

Figure. S8. Cycling stability of MNFHCF–631//HC full cells cycled at 0.2 C in the voltage range of 1.5–4.0 V.

Full cell performance was tested using MNFHCF–631 (cathode) and hard carbon (anode). Full cell assembly conditions were discussed in the experimental electrochemical measurement part. The initial discharge capacity was 99.52 mAh/g, and the initial Coulombic efficiency (ICE) was 81.8 %. The Coulombic efficiency gradually increased during cycling. The capacity was maintained at 84.83 % after 20 cycles. Full cells exhibit lower cycling stability than half cells. This is possibly due to the relatively low initial coulombic efficiency of hard carbon (HC) and inadequate capacity matching between cathode and anode or electrolyte not suitable for full cell.[9,10] However, this MNFHCF–631 short cycle performance demonstrated smooth operation even in full cell conditions. Further work will be carried out to optimize the full cell condition.

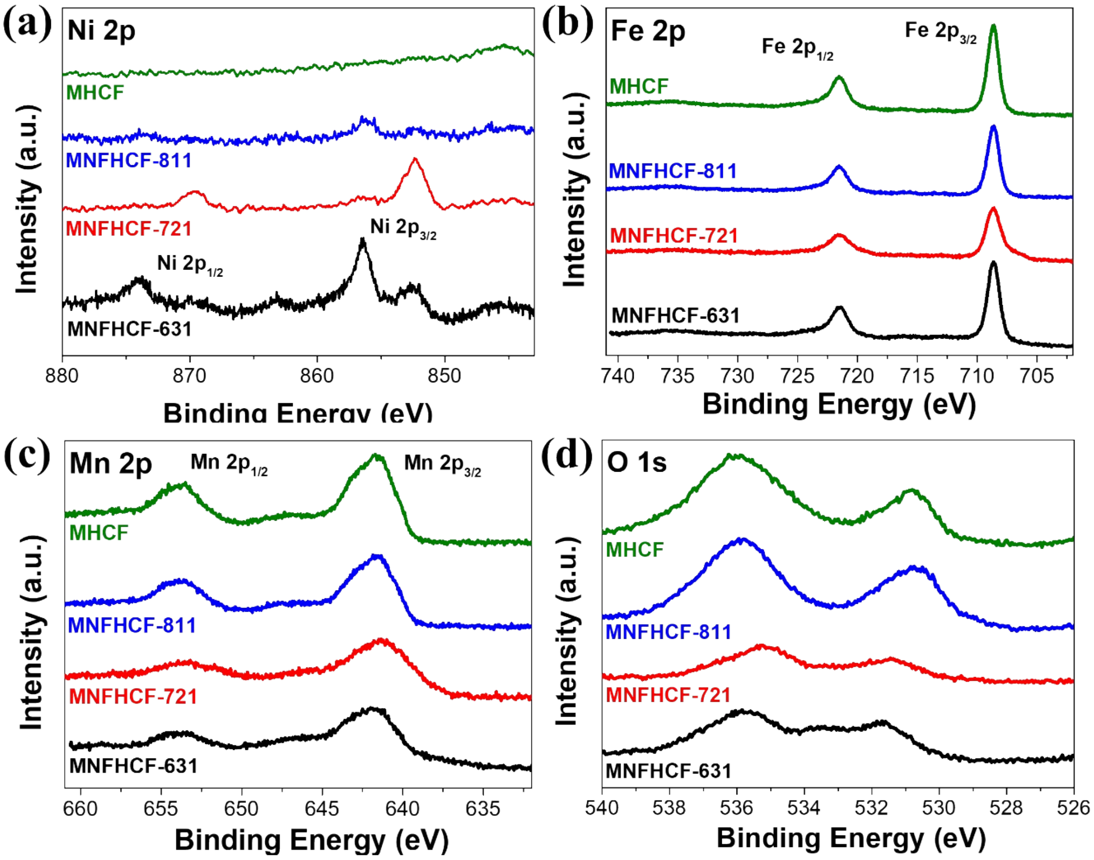

Figure. S9. (a) Ni 2p, (b) Fe 2p, and (c) Mn 2p (d) O 1s spectra of MHCF, MNFHCF–631, MNFHCF–721, MNFHCF–811.

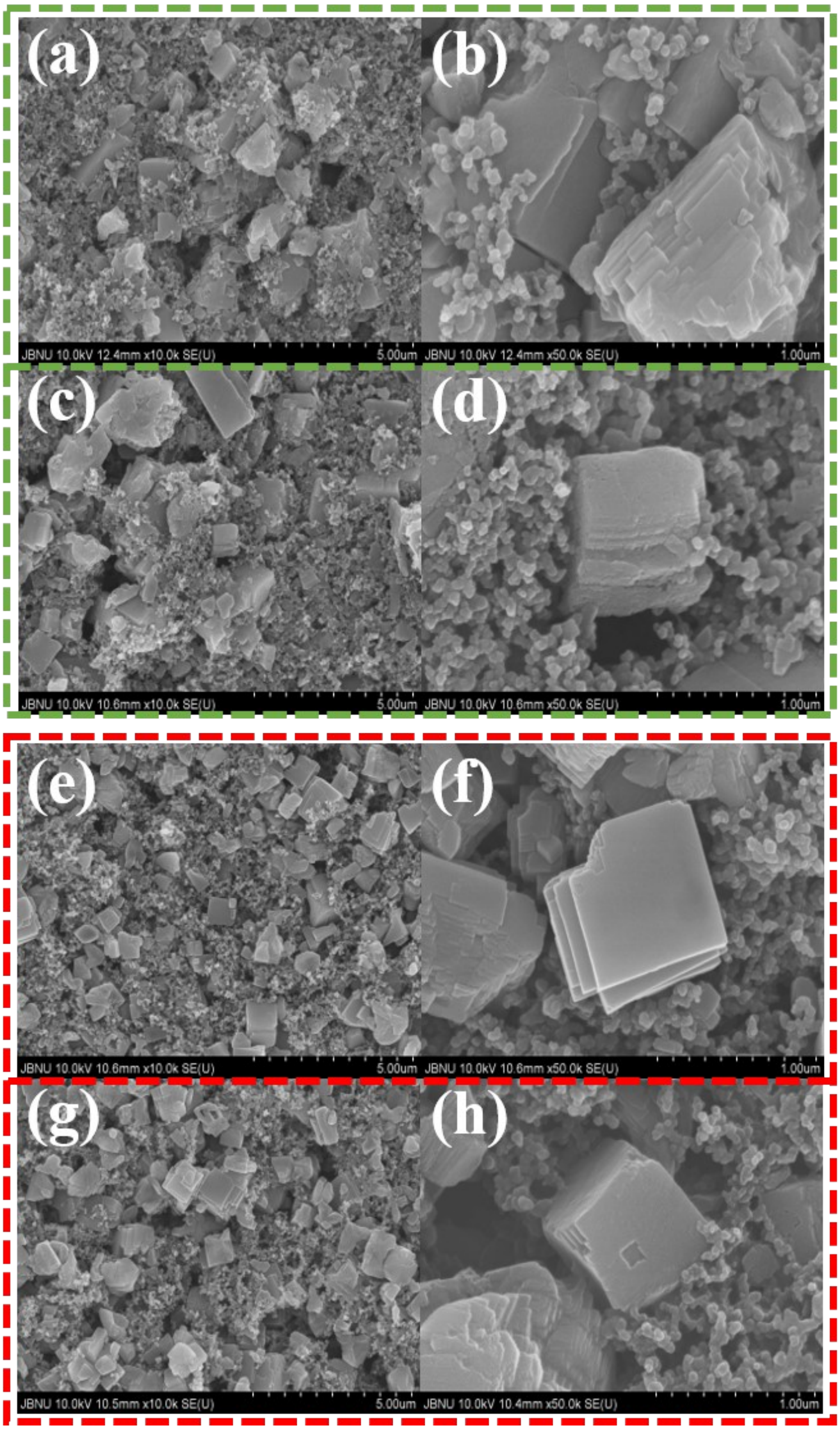

Figure. S10. FESEM images of particles in the electrode of (a-b) MHCF before cycling, (c-d) MHCF after 100 cycling, (e-f) MNFHCF–631 before cycling, and (g-h) MNFHCF–631 after 100 cycling.

Reference

[1] J. Li, L. Liu, Y. Gao, J. Guo, X. Long, S. Chen, S. Yang, Q. Yuan, Y. Sun, Z. Lan, Y. Liu, X. Zhou, Y. Jiang, *Mater. Sci. Eng. B.*, 2025, **318**, 118308.

[2] L. Xu, M. Chen, G. Chen, H. Wu, W. Wu, X. Wu, *Chem. Eng. J.*, 2024, **497**, 154551.

[3] J. Li, X. He, S. Ostendorp, L. Zhang, X. Hou, D. Zhou, B. Yan, D. M. Meira, Y. Yang, H. Jia, G. Schumacher, J. Wang, E. Paillard, G. Wilde, M. Winter, J. Li, *Electrochim. Acta.*, 2020, **342**, 135928.

[4] J. Wang, Z. Wang, H. Liu, J. Gao, Y. Xu, Z. Chen, X. Li, Y. Liu, *Electrochim. Acta.*, 2023, **448**, 142183.

[5] Y. Luo, J. Shen, Y. Yao, J. Dai, F. Ling, L. Li, Y. Jiang, X. Wu, X. Rui, Y. Yu, *Adv. Mater.*, 2024, **36**, 2405458.

[6] D. A. E.-Hady, Y. Lyu, S. Zhan, J. Yang, Y. Wang, F. Yang, Q. Zhao, M. Gu, M. Shao, *ACS Appl. Energy Mater.*, 2022, **5**, 8547–8553.

[7] M. O. Tolentino , M. González M , H. Osiry , G. R. Sánchez and I. González , *Dalton Trans*., 2018, **47**, 16492–16501.

[8] H. Fu, C. Liu, C. Zhang, W. Ma, K. Wang, Z. Li, X. Lu, G. Cao *J. Mater. Chem. A*, 2017, **5**, 9604–9610.

[9] W. Li, C. Han, W. Wang, Q. Xia, S. Chou, Q. Gu, B. Johannessen, H. Liu, and S. Dou, *Adv. Energy Mater.*, 2020, **10**, 1903006.

[10] N. LeGe, X. -X. He, Y. -X. Wang, Y. Lei, Y. -X. Yang, J. -T. Xu, M. Liu, X. Wu, W. -H. Lai and S. -L. Chou, *Energy Environ. Sci.*, 2023, **16**, 5688–5720.